

# Calibration of X-ray absorption in our Galaxy

R. Willingale<sup>\*</sup>, R.L.C. Starling, A.P. Beardmore, N.R. Tanvir and P.T. O’Brien

*University of Leicester, Department of Physics and Astronomy, University Road, LE1 7RH, UK*

Accepted Received ; in original form

## ABSTRACT

Prediction of the soft X-ray absorption along lines of sight through our Galaxy is crucial for understanding the spectra of extragalactic sources, but requires a good estimate of the foreground column density of photoelectric absorbing species. Assuming uniform elemental abundances this reduces to having a good estimate of the total hydrogen column density,  $N_{Htot} = N_{HI} + 2N_{H_2}$ . The atomic component,  $N_{HI}$ , is reliably provided using the mapped 21 cm radio emission but estimating the molecular hydrogen column density,  $N_{H_2}$ , expected for any particular direction, is difficult. The X-ray afterglows of GRBs are ideal sources to probe X-ray absorption in our Galaxy because they are extragalactic, numerous, bright, have simple spectra and occur randomly across the entire sky. We describe an empirical method, utilizing 493 afterglows detected by the *Swift* XRT, to determine  $N_{Htot}$  through the Milky Way which provides an improved estimate of the X-ray absorption in our Galaxy and thereby leads to more reliable measurements of the intrinsic X-ray absorption and, potentially, other spectral parameters, for extragalactic X-ray sources. We derive a simple function, dependent on the product of the atomic hydrogen column density,  $N_{HI}$ , and dust extinction,  $E(B - V)$ , which describes the variation of the molecular hydrogen column density,  $N_{H_2}$ , of our Galaxy, over the sky. Using the resulting  $N_{Htot}$  we show that the dust-to-hydrogen ratio is correlated with the carbon monoxide emission and use this ratio to estimate the fraction of material which forms interstellar dust grains. Our resulting recipe represents a significant revision in Galactic absorption compared to previous standard methods, particularly at low Galactic latitudes.

## 1 INTRODUCTION

Understanding the soft X-ray spectra of extragalactic sources requires an estimate of the foreground photo-electric absorption due to gas and dust in the Milky Way. The total photo-ionization cross-section which gives rise to X-ray absorption in the ISM can be written as the sum of contributions from 3 phases

$$\sigma_{ISM} = \sigma_{gas} + \sigma_{molecules} + \sigma_{dust}. \quad (1)$$

It is conventional to normalise the cross-section with respect to the total hydrogen column density,  $N_{Htot} \text{ cm}^{-2}$  (molecular, neutral atomic and ionized), such that the X-ray spectrum observed at energy  $E$  is

$$I(E) = \exp(-\sigma_{ISM}(E)N_{Htot})I_0(E) \quad (2)$$

where  $I_0(E)$  is the source spectrum. Absorption in the soft band, 0.1-2 keV, is included in spectral fitting using a detailed model of the cross-section,  $\sigma_{ISM}$ , and the hydrogen column density,  $N_{Htot}$ , is usually a fitted parameter. The cross-sections for each of the phases are obtained by summing the photo-ionization cross-sections of the individual constituent atoms and ions weighting their contributions by the abundances. Following the notation in Ride & Walker (1977) the cross-section for the gas phase can be written as

$$\sigma_{gas} = \sum_{Z,i} A_Z \times a_{Z,i} \times (1 - \beta_{Z,i}) \times \sigma_{Z,i}, \quad (3)$$

where the relative abundance of element  $Z$  with respect to hydrogen is  $A_Z = N_Z/N_{Htot}$  and the fraction of ions of this element in the  $i^{th}$  ionization state is  $a_{Z,i} = N_{Z,i}/N_Z$  and  $\sigma_{Z,i}$  is the total photo-ionization cross-section of this ionization state. The fraction of ions in the gas phase is  $1 - \beta_{Z,i}$  so  $\beta_{Z,i}$  is the fraction in other phases (usually dominated by the fraction in dust grains). Atoms deep within large grains are shielded by the outer layers and therefore their contribution to the total cross-section is reduced. Similarly, some atomic absorption edges are modified if the atoms are incorporated into molecules and the molecular cross-section is not a simple sum of the cross-sections of the constituent atoms/ions. If the ISM is warm then higher ionization states are excited and the  $a_{Z,i}$  values will be modified. But all these factors only introduce small changes and what really dominates the total cross-section are the abundances of the atomic types,  $A_Z$ . It is usually assumed that these abundances have fixed values across the Galaxy and so if we fix the value of  $N_{Htot}$  the column densities of all other atomic types can be determined and the expected cross-sections can be estimated. Apportioning these atoms between atomic gas, partially ionized gas, molecules and dust will normally introduce only minor perturbations to the total cross-section. Further de-

tails about this model of X-ray absorption in the ISM are given by Wilms et al. (2000).

For extragalactic X-ray sources we can split the total measured absorption into two components including both the column density in our Galaxy,  $N_{H,g}$ , and the excess column density in the host galaxy or elsewhere,  $N_{H,i}$ . If we know the redshift of the host then we can express the excess column in the rest frame of the host. However, if the spectral resolution is modest then individual absorption line features will not be visible and the energy profile of absorption is not expected to be a strong function of redshift meaning we cannot fit both components simultaneously. We must fix  $N_{H,g}$  if we want to extract a meaningful estimate of  $N_{H,i}$ . Therefore fitted values of the excess absorption for extragalactic sources are critically dependent on our understanding of  $\sigma_{ISM}$  and  $N_{H,g}$  for different lines of sight through our Galaxy.

The dominant fraction of the total hydrogen column density is atomic,  $N_{HI}$ , (approximately 80% on average Wilms et al. 2000) and this is readily estimated using 21 cm radio emission maps (e.g. the Leiden-Argentine-Bonn (LAB) survey Kalberla et al. (2005)). However, mapping the distribution of molecular hydrogen throughout our Galaxy is difficult. The molecule has no permanent dipole which makes any radiative transitions weak and hard to detect. Surveys in the near-infrared using the  $H_2$  line emission at  $2.122 \mu\text{m}$  (like *UWISH2*, Froebrich et al. (2011)) readily detect dense ( $n_{H_2} > 10^3 \text{ cm}^{-3}$ ) giant molecular clouds and supernova remnants but fail to detect diffuse emission from the low density interstellar medium (ISM) ( $n_H \sim 1 \text{ cm}^{-3}$ ) because of the surface brightness limit,  $\sim 10^{-19} \text{ W m}^{-2} \text{ arcsec}^{-2}$ , and the presence of numerous stars. Molecular hydrogen in the ISM is most readily observed using absorption lines from the first six rotational levels ( $J = 0-5$ ) seen in the ultraviolet between 900 and 1130 Å. A sparse map of the column density,  $N_{H_2}$  molecules  $\text{cm}^{-2}$ , across the Galaxy has been produced using *FUSE* UV spectroscopy on 73 extragalactic targets, (Wakker 2006), but with so few lines of sight it is difficult to construct a reliable and detailed picture. Furthermore all the targets considered were at high Galactic latitude with a maximum total hydrogen column density of  $\sim 10^{21} \text{ cm}^{-2}$  so the distribution at high density in or near to the Galactic plane is not included. These data indicate that the molecular fraction of the column density along the line of sight, defined as

$$f(H_2) = \frac{2N_{H_2}}{N_{HI} + 2N_{H_2}}, \quad (4)$$

is highly variable at high Galactic latitudes and is not tightly correlated with the atomic gas column density,  $N_{HI}$  atoms  $\text{cm}^{-2}$ , or the total hydrogen column.

The afterglow emission of Gamma Ray Bursts (GRBs) is seen at all wavelengths from X-ray through to radio and is thought to be synchrotron radiation arising from the shock produced when the GRB jet impacts the surrounding medium (e.g. Meszaros & Rees (1992); Sari et al. (1998)). The X-ray emission (0.3-10 keV) from GRB afterglows is routinely measured today by the *Swift* satellite (Gehrels et al. 2004) and in almost all cases the soft X-ray spectrum is well modelled by a simple power law continuum modulated by photoelectric absorption at low energies. Absorption is expected from gas in the Milky

Way along the line of sight but for most *Swift* GRBs there is also evidence for significant absorption in excess of the Galactic foreground. This is attributed to gas in the host galaxy and/or intergalactic clouds along the line of sight and has been studied in detail by many authors, see Behar et al. (2011); Campana et al. (2012); Schady et al. (2011); Watson (2011); Zafar et al. (2011) and references therein. Because the X-ray afterglows are bright and have simple continuum spectra they provide an excellent opportunity to study the cold absorbing material in our Galaxy as well as the ISM in the distant host galaxies and this is what we turn attention to here.

## 2 FITTING GRB X-RAY AFTERGLOW SPECTRA

We selected X-ray afterglow spectra measured by the *Swift* X-ray Telescope (XRT) in photon counting (PC) mode from GRBs up until 2011 November 3. We did not use data obtained in Windowed Timing (WT) mode to avoid, as far as possible, early times post-burst when spectral evolution, probably associated with the prompt emission, is most likely to be occurring. For a few GRBs there is evidence for an additional, early, thermal continuum component which is probably associated with the prompt emission or a supernova (SNe) rather than the afterglow. One such object for which extensive PC mode data were obtained is GRB 060218 (Campana et al. 2006) and we excluded this from our sample. GRB 090618 (Page et al. 2011), GRB 100316D (Starling et al. 2011) and GRB 101219B (Starling et al. 2012) have similar early spectra but such complications are only seen in WT mode so these were included in our analysis. We fitted the GRB afterglow spectra with a simple model comprising a power-law continuum specified by two fitted parameters, a photon index and a normalisation, and two absorption components representing the Galactic absorbing column (with fixed column density) and the excess absorbing column for which the column density was allowed to float. The  $N_{H,g}$  values used were taken from the LAB 21 cm all-sky survey, Kalberla et al. (2005), using the FTOOLS NH procedure on the GRB positions. Fig. 1 shows the values for the fixed Galactic,  $N_{H,g}$ , and fitted excess  $N_{H,i}$ , column densities from spectral fits of 493 afterglows.

The fitting was done using XSPEC version 12.7.0 (Arnaud 1996) utilizing the absorption model tbabs<sup>1</sup>, Wilms et al. (2000). This model includes elemental abundances tabulated by the same authors and these abundances were used for all the spectral fitting reported below except for those cases mentioned explicitly in the text. The  $N_{H,i}$  values plotted are the fitted values (excess absorption over and above the fixed Galactic value) assuming a redshift of zero (even for those bursts for which we know the redshift). We note that in this paper we are not concerned with the physical origin of the excess absorption in GRB afterglow spectra, and using the complete set, irrespective of whether

<sup>1</sup> The XSPEC command variants ztbabs and tbvarabs were also used extensively in the analysis to provide direct access to the abundance, dust grain and redshift parameters.

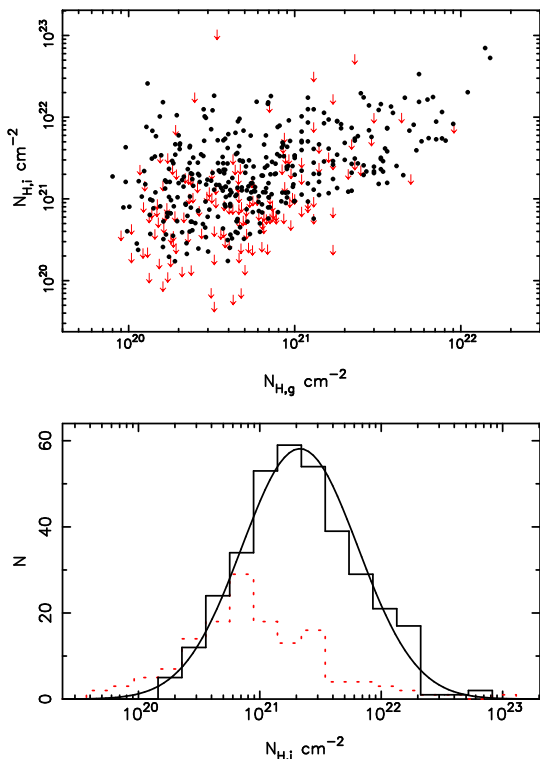


**Figure 1.** The results from fitting 493 individual GRB afterglow spectra. Top panel: The fitted values of excess hydrogen column  $N_{H,i}$  (assuming  $z = 0$ ) plotted against the fixed values of  $N_{H,g}$ . Upper limits (3 sigma) for  $N_{H,i}$  are shown as arrows. No correlation is expected between these two column densities but even allowing for the upper limits it is clear that  $N_{H,i}$  is systematically increasing with  $N_{H,g}$ . We note that a Galactic column density of  $N_{H,g} = 10^{21} \text{ cm}^{-2}$  corresponds to a average Galactic latitude of -13 degrees in the South and +22 degrees in the North. Some 29% of the sky has  $N_{H,g} > 10^{21} \text{ cm}^{-2}$ . Bottom panel: The distribution of fitted  $N_{H,i}$ . The smooth curve is a log-normal fit to the distribution. The dotted histogram shows the distribution of the upper limits.

a redshift has been determined, provides a much larger sample for the analysis and removes any risk of optical bias. The underlying GRB redshift distribution should, of course, be independent of position with respect to the Galaxy. The paucity of points in the bottom right of the plot is not immediately surprising because if the Galactic column is high the sensitivity to an excess column is reduced. We would expect the points from the lower-right (low  $N_{H,i}$  and high  $N_{H,g}$ ) to become upper limits in the upper-right of the distribution. In fact there are very few upper limits for objects with high  $N_{H,g}$  and for these values the fitted  $N_{H,i}$  are higher than average. The distribution of fitted  $N_{H,i}$  values is shown in the bottom panel. The observed distribution is slightly skewed with respect to the log-normal fit and there appears to be an excess bump in the high tail. The distribution has a mean value of  $2.1 \times 10^{21} \text{ cm}^{-2}$  and a rms width of 0.48 dex.

Although the X-ray afterglows of GRBs are exceptionally bright compared with other extragalactic sources, they are only visible over a relatively short time window and the spectra of some bursts have limited statistics, which of course is ultimately the reason for the upper limits on excess

absorption for many GRBs. The distribution of upper limits is shown relative to the whole distribution in the lower panel of Fig. 1. They are clearly biased towards the lower tail of the  $N_{H,i}$  distribution, as expected, and we need some way of including these lower limits in our analysis if we are to understand what is going on. In order to investigate further we sorted the bursts into ascending order of  $N_{H,g}$  and selected GRBs in groups of 26, each group containing bursts that are expected to suffer a similar degree of Galactic absorption. This gave 18 groups of 26 and a final 19th group of 25. We summed together the count spectra in each group to produce 19 composite spectra and then fitted each composite spectrum using XSPEC. Tools are provided along with XSPEC to sum the source spectra, background files, the area files (ARFs) and the response files (RMFs) to facilitate accurate fitting of composite spectra. The component spectra from the GRBs were extracted using grade 0-12 events from PC mode and the appropriate ARF and RMF files were automatically selected for the correct epoch. We didn't apply any binning to the raw spectra because the composite spectra contained more than adequate counts. Pile-up was avoided by excising the core of the PSF when appropriate. The ARF files were summed weighting by the total counts in the spectrum. It was found that only two significantly different RMF files were required, before and after the substrate voltage change which was performed 2007-09-01. We summed these weighting by the accumulated time before and after the change over date. We checked this summing procedure using different weightings and different combinations of ARFs and RMFs. Because each group contains 26 GRBs the results were remarkably insensitive to the weightings or components used. The average photon index of the power law continuum fitted for the individual GRBs was  $\Gamma = 1.96$  and the rms scatter was small, 0.18. We therefore expect the continua of the composite spectra to be well represented by a simple power law (with similar photon index) and we fitted the composite spectra using the same model as used for the individual GRBs. We fixed the redshift for the excess column as  $z = 0$  and fixed the  $N_{H,g}$  to the mean for each group. Because the range of  $N_{H,g}$  within each group is narrow small changes in the fixed  $N_{H,g}$  values used make no difference to the results. The mean value of the excess absorbing column density required increases with redshift but, crucially, the quality of the fit and the scatter of the excess absorption column densities remain the same.

Fig. 2 shows the fitted  $N_{H,i}$  values for the 19 groups plotted against the fixed  $N_{H,g}$  values. Following the conventional approach, already used for the fits shown in Fig. 1, we used the  $N_{H,g}$  values taken from the LAB 21 cm all-sky survey. The error bars in  $N_{H,g}$  indicate the range of Galactic absorption within each group while those in  $N_{H,i}$  represent the 90% range for the fitted values. Crucially all the groups return a well defined  $N_{H,i}$  value with a 90% range and there are no upper limits. We expect there to be no correlation between the excess absorption in the GRBs and the column density within our Galaxy but the result of fitting the groups clearly indicates a strong trend. We can quantify the significance of the trend by calculating a reduced Chi-squared value against a constant model for  $N_{H,i}$ ,  $\chi^2_{\nu} = 64.4$ . In evaluating  $\chi^2$  we use the formal fitting errors, although this will underestimate the true uncertainties given the random variation in the GRB afterglow properties from group

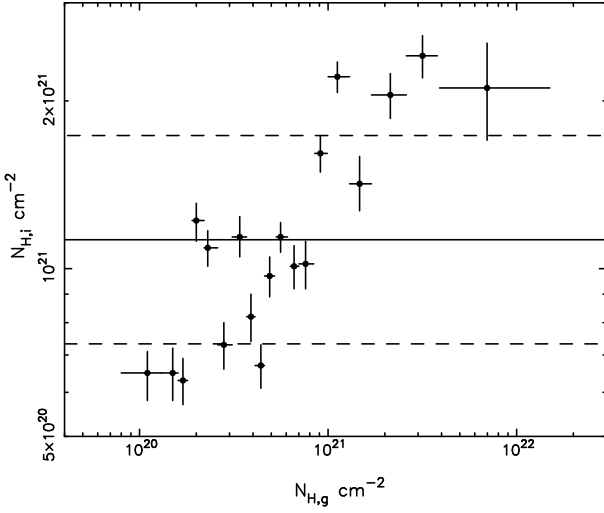


**Figure 2.** The fitted values of  $N_{H,i}$ ,  $z = 0$ , for 19 GRB groups plotted against the fixed values of Galactic hydrogen column  $N_{H,g}$ . The solid horizontal line indicates the geometric mean and the dashed lines  $\pm 1$  sigma in dex.

to group. Assuming the width of the distribution of  $N_{H,i}$  values in Fig. 1 is representative of the GRB population, convolved with the measurement errors, we expect the rms between groups of 26 GRBs to be  $\approx 0.09$  dex. Using this we can estimate the contribution to reduced Chi-squared from the scatter in  $N_{H,i}$  giving an expected value of reduced Chi-squared as  $\langle \chi^2_\nu \rangle = 17.3$ . The trend is obviously significant. Using linear regression we estimate that the total swing in the  $N_{H,i}$  values fitted across the full range of  $N_{H,g}$  values in the groups is a factor of 6.0. Either there is something wrong with the calibration of the data, the spectral fitting procedure is faulty or the model for the Galactic absorption is incorrect.

There is a spread of GRB brightnesses within each group but if only one or two GRBs were to dominate this might bias the results. In fact the brightest GRB in each group contributes somewhere in the range 10-15% of the total count so a single GRB is not dominant in any group. However the distribution of brightnesses of the GRBs in each group is obviously important. It reduces the effective number of GRBs contributing to the averaging and thereby increases the scatter we expect from the redshift dependence and intrinsic spread in  $N_{H,i}$  values. We return to this point later and show that the chosen grouping of the GRBs does not bias the results.

We inspected all the group fits to check for anomalies. Fig. 3 shows the count rate spectrum and fitted profile for the 16<sup>th</sup> group which is typical of the groups with  $N_{H,g} > 10^{21} \text{ cm}^{-2}$ . The solid curve is the best fit including the fixed Galactic column,  $N_{H,g}$  and the fitted excess column,  $N_{H,i}$ . The statistics are excellent and there are no features or large residuals to suggest a fault with the calibration or the fitting procedure. The dashed line is the predicted spectrum with the excess absorption component set to zero,  $N_{H,i} = 0$ . The count rate residuals are shown in the lower panel. The excess absorption signature is clearly significant and covers a wide range of the low energy bins. For the GRB groups with  $N_{H,g} < 10^{21} \text{ cm}^{-2}$  the excess ab-

sorption signature is much larger than the example shown in Fig. 3.

The XRT calibration influences the fitting of the absorption component in three ways. The first and dominant factor is the roll-off of the efficiency below  $\sim 1.0$  keV. If the efficiency roll-off is too shallow then the fitted column density must increase to match the detected count rate profile. Conversely, if the roll-off is too steep, the fitted column density will be too low. The second factor is the broad efficiency profile and, in particular, the roll-off of the efficiency above  $\sim 2$  keV and the ratio of the collecting area at high energies, above  $\sim 2$  keV, to that at low energies, below  $\sim 1$  keV. These factors determine the profile of the power law continuum spectrum. If the high energy roll-off is too shallow then the fitted spectral index will be too large and the fitted column density must increase to compensate. Conversely, if the fitted index is too small then the fitted column density will be too small. The third factor is the redistribution matrix which dictates the detailed shape of the predicted count distribution. Any mismatch between the predicted and observed count profile degrades the goodness of fit and can lead to systematic errors in the fitted parameters including the column density.

According to the latest XRT calibration release note (version 16) a systematic error of  $\sim 3\%$  is required when fitting high statistical quality spectra using the current RMF and ARF response files. Including such a systematic error has no effect on the results plotted in Fig. 2. The magnitude of the absorption fitted depends on the area calibration as a function of energy, in particular over the low energy range 0.3-1.5 keV. If the roll-off of this area set by the calibration is incorrect, the absorption will be over- or under-estimated accordingly as discussed above. In order to determine the sensitivity of the fitted  $N_{H,i}$  results reported throughout this work we repeated all the analysis with three versions of the *Swift* XRT calibration. Firstly the currently released version (SWIFT-XRT-CALDB-09\_v16) and secondly two trial versions generated by employing plausible enhancements of the known uncertainties in the hardware calibration: the detector QE, the filter transmission using updated absorption coefficients and measurements and mirror X-ray reflectivity incorporating a contaminating carbon overcoat. The trial calibrations comprise both new RMF and ARF files. A comparison of the areas for these calibrations is shown in Fig. 4. Significant differences are the depth of the oxygen K-edge at  $\sim 0.54$  keV and the detailed structure across the silicon K-edge at  $\sim 1.8$  keV and the gold M-edges 2.2 – 4.0 keV. The trial1 and trial2 curves in Fig. 4 have been scaled so that the differences in the roll-off at low energies is most obvious. For trial1 the roll-off below 1 keV is  $\sim 20\%$  shallower than the current calibration and for trial2 this roll-off is  $\sim 20\%$  steeper. The differences between the true calibration and either version 16, trial1 or trial2 are very unlikely to be greater than the differences visible in Fig. 4. We note that the trial XRT calibrations are not intended as a better approximation to the true state of the instrument but they serve to illustrate that significant changes to the effective area calibration do not alter our results. Using the trial1 XRT calibration increases the fitted  $N_{H,i}$  values by around 25% and the total swing in the  $N_{H,i}$  values fitted across the full range of  $N_{H,g}$  values in the groups is a factor of 5.7, a little less than the swing using the current cali-

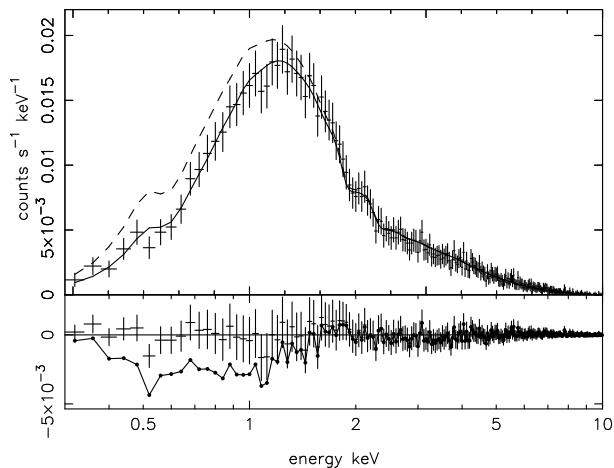


**Figure 3.** Top panel: The measured count spectrum for the 16<sup>th</sup> composite group. The solid line indicates the best fit model. The dashed line shows the model prediction when  $N_{H,i} = 0$ . Bottom panel: The count rate residuals. The solid curve and dots show the residuals when  $N_{H,i} = 0$ .

bration (6.0). Using the trial2 decreases the fitted  $N_{H,i}$  by around 20% and increases the swing factor to 10.4, somewhat larger than for the current calibration. In addition to these extreme versions of the calibration we also tried varying the RMFs and ARFs individually through intermediate values. These changed the results in the same sense as trial1 or trial2 although the changes were always smaller.

The primary influence of all the calibration factors on the fitted column density is a simple scaling because the instrument response and the fitting procedure are, essentially, linear. If we change the roll-off in the effective area below  $\sim 1$  keV by 10% then we expect the fitted  $N_H$  to change by  $\sim 10\%$ . This scaling is independent of the absolute value of  $N_H$ . However, the trend in the fitted column density values which we are trying to account for is not the result of a simple scaling error. We conclude that uncertainties in the calibration cannot account for the observed trend seen in Fig. 2, and we believe that the XSPEC fitting procedure is well tried and tested.

### 3 MODIFYING THE GALACTIC ABSORPTION MODEL PARAMETERS

#### 3.1 Global scaling

The default implementation of the Wilms et al. (2000) ISM model in the XSPEC tbabs model includes a molecular hydrogen fraction,  $f(H_2)$  as defined in Equation 4, of 20%. It assumes that the  $N_{H,tot}$  fit parameter is the sum of the column densities (both expressed in terms of hydrogen atoms per unit area) of  $HI$  and  $H_2$ . Therefore, employing the widely adopted conventional approach and setting  $N_{H,tot} = N_{HI}$  from 21 cm surveys is strictly an incorrect use of this routine. The measured  $HI$  column should be multiplied by 1.25 so that 20% represents the molecular column and 80% the  $HI$  fraction. Fig. 5 shows the distribution of fitted  $N_{H,i}$  if we adopt this value for the Galactic column in the group spectral fitting. The bursts in the last (19th) group

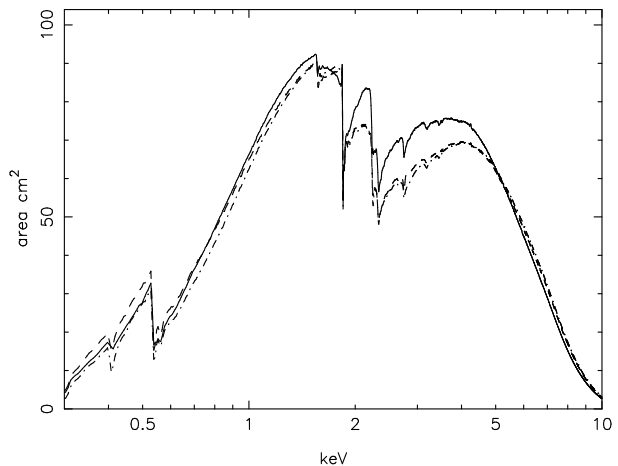


**Figure 4.** Comparison of the effective area as a function of energy for the current (version 16) XRT calibration (solid curve), our trial1 calibration (dashed line), and our trial2 calibration (dot-dashed line). The trial1 and trial2 values have been scaled so all three curves have the same area at  $\sim 1.85$  keV.

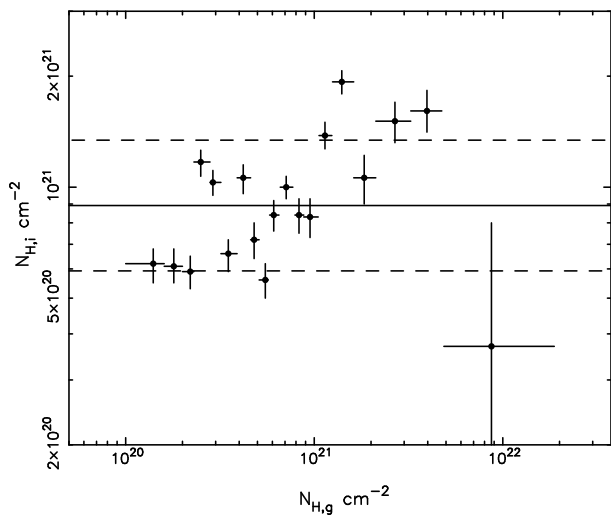


**Figure 5.** The  $N_{H,i}$  values for the 19 GRB groups using  $N_{H,g}$  equal to  $1.25 \times N_{HI}$ . The apparent discrepancy between the bin to bin scatter and the 90% error bars may not be very surprising, given that each group contains GRBs at a range of redshifts and true (intrinsic) columns. The horizontal lines are as in Fig. 2.

have a very high mean foreground  $N_{H,g} \sim 10^{22} \text{ cm}^{-2}$ , and are typically at galactic latitudes  $< 2.0$  degrees. Thus their lines of sight pass through complex regions of the disk, and it would be rather surprising if estimates of the foreground absorption were at all accurate. Nonetheless, in Fig. 5 the 19th group is, within the large formal errors, consistent with the  $N_{H,i}$  value for the low foreground bins. The remaining groups still show the same unexplained trend as before. The reduced Chi-squared is now  $\chi^2_\nu = 40.9$  while the expected value is  $< \chi^2_\nu > = 13.5$ . If the trial1 calibration described in Section 2 is used Fig. 5 is very similar except the mean value of  $N_{H,i}$  is increased by 25%. The trial2 calibration decreases the mean value by 18%.

A simple scaling of the measured  $N_{HI}$  column density (or equivalently including a fixed percentage for molecular

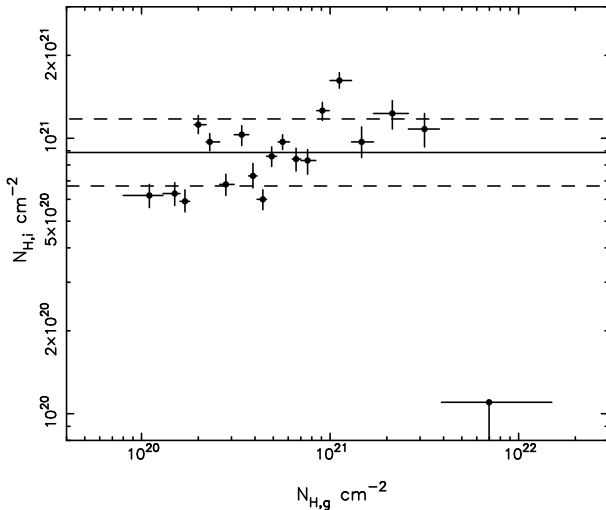


**Figure 6.** The  $N_{H,i}$  values for the 19 GRB groups obtained using the abundances of Anders & Grevesse (1989). The horizontal lines are as in Fig. 2.

hydrogen) is unable to explain the apparent variation in excess GRB column density as a function of the absorbing column in our Galaxy. An alternative explanation for the apparent variation might be an error in the elemental abundances assumed. The Wilms et al. (2000) model includes updated abundances which are approximately 70% of the previously widely used values from Anders & Grevesse (1989). To test the effect of this change we re-ran the group fitting using the Anders & Grevesse (1989) abundances for the  $N_{H,g}$  component. The result is shown in Fig. 6. The apparent variation remains and the Galactic absorption used for the top  $N_{H,g}$  group is now too large and results in an upper limit which is lower than the fitted values for all the other groups. Using the trial calibrations to produce Fig. 6 makes little difference. Using trial1 the  $N_{H,i}$  value for the 19<sup>th</sup> group is still too low but somewhat higher and closer to the average value. If the trial2 calibration is used then the 19<sup>th</sup> is near the average value but  $N_{H,i}$  for the lower  $N_{H,g}$  drop away in the same trend as Fig. 5.

We also tried varying the global percentage of molecular hydrogen from 0 to 30% and varying the elemental abundances between values consistent with Wilms et al. (2000) and Anders & Grevesse (1989) but no combination improved the situation. We conclude that the problem is not resolved by a simple scaling of either the hydrogen density or the elemental abundances independent of position on the sky. What is required is a modification of the ISM model as a function of direction across the Galaxy. In particular the absorption associated with the mid-range values of  $N_{H,g}$ , around  $10^{21} \text{ cm}^{-2}$ , needs to be increased while the lowest and the very highest absorption values should remain as they are. In all the subsequent analysis we reverted to using the abundances given in Wilms et al. (2000).

### 3.2 The column density of molecular hydrogen as a function of $N_{HI}$

The fraction of hydrogen in molecular form is known to be highly variable (e.g. Rachford et al. 2002). In order to get

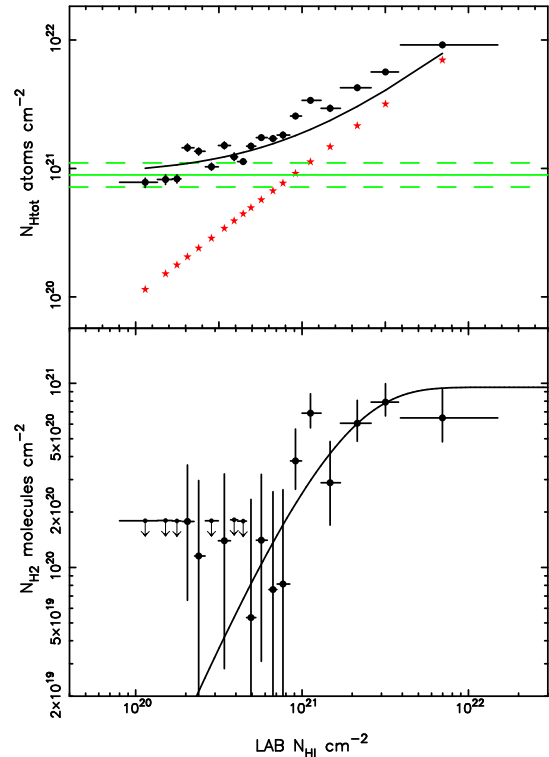


**Figure 7.** Upper panel: The fitted total hydrogen column densities,  $N_{H,tot}$ , for the 19 group spectra plotted vs. the  $N_{HI}$  average for each group. The stars show the  $N_{HI}$  component (from the LAB survey) and the horizontal lines indicate the mean and rms range of the expected excess column density component,  $N_{H,i}$ , constant across all groups. The solid rising curve is the sum of LAB  $N_{HI}$  and  $N_{H,i}$ . Lower panel: The  $N_{H_2}$  column density derived by subtracting the Galactic HI and excess HI contributions from the total. Those  $N_{H_2}$  values plotted with downward pointing arrows are upper limits. The solid curve shows the simple model adopted for the molecular hydrogen column density as a function of the HI column density.

a handle on the possible variation in the column density of molecular hydrogen we fitted the 19 group spectra with a single absorption component giving a total column density estimate,  $N_{H,tot}$ , for each group. This fitted total is expected to be the sum of the Galactic and excess components. Fig. 7 shows these single fitted values as a function of the average LAB survey  $N_{HI}$  values for each group. We expect  $N_{H,tot}$  to be the sum of contributions from Galactic  $N_{HI}$ , excess  $N_{H,i}$  and Galactic  $N_{H_2}$ . The lower panel shows the estimate of  $N_{H_2}$  obtained by subtracting the other two components from the total. To produce these values we assumed that the excess component has a mean of  $9.4 \times 10^{20} \text{ cm}^{-2}$  (which is the average for the first 4 groups and very close to  $8.9 \times 10^{20} \text{ cm}^{-2}$  given by the results in Fig. 5) and an rms value estimated from the width of the distribution from the individual fits shown in Fig. 1. For  $N_{HI} > 10^{21} \text{ cm}^{-2}$  the putative molecular hydrogen column is high and constant, independent of  $N_{HI}$ , and below this it drops away although it is difficult to determine the functionality of the decline because the sensitivity is limited by the intrinsic scatter of the  $N_{H,i}$  values for the individual GRBs. Note that 6 of the groups below  $N_{H,g} = 5 \times 10^{20} \text{ cm}^{-2}$  have  $N_{H_2}$  values which

are upper limits. We repeated the analysis summarised in Fig. 7 using the trial1 calibration described in Section 2. The  $N_{Htot}$  values returned were  $2.2 \times 10^{20} \text{ cm}^{-2}$  higher, averaged across all groups. For groups with  $N_{Htot} < 1.5 \times 10^{21} \text{ cm}^{-2}$  this corresponds to an average increase of 16% while for those with  $N_{Htot} > 1.5 \times 10^{21} \text{ cm}^{-2}$  the average increase is 8%. We had to increase the assumed mean value of the excess component to  $1.1 \times 10^{21} \text{ cm}^{-2}$ , in line with the trial1 calibration results returned when plotting Fig. 5, but the estimated  $N_{H2}$  values in the lower panel were the same within the limits imposed by the error ranges plotted. Using the trial2 calibration shift things in the opposite direction with  $N_{Htot} \sim 18\%$  down but otherwise the result is the same. This confirms that the excess Galactic absorption, attributed to the molecular hydrogen column density in Fig. 7, is not an artifact of uncertainties in the calibration. It also demonstrates that the limits of uncertainties in the calibration introduce a systematic error of  $\sim 16\%$  in the total fitted column density for low columns and  $\sim 8\%$  when  $N_{Htot} > 1.5 \times 10^{21} \text{ cm}^{-2}$ .

Given the results plotted in Fig. 7 we initially assumed that the molecular hydrogen column density throughout the Galaxy has the profile indicated by the solid line plotted in lower panel of Fig. 7. This has the form

$$N_{H2} = N_{H2max} \left[ 1 - \exp \left( \frac{-N_{HI}}{N_c} \right) \right]^\alpha \quad (5)$$

and we set the total Galactic hydrogen column density as

$$N_{H,g} = N_{HI} + 2N_{H2} \quad (6)$$

taking  $N_{HI}$  from the LAB 21 cm survey. If  $N_{HI} \ll N_c$  then  $N_{H2}$  approximates to a simple power law with index  $\alpha$  and if  $\alpha = 1$ ,  $N_{H2}$  is a simple fraction of  $N_{HI}$ . If  $N_{HI} \gg N_c$  then  $N_{H,g}$  asymptotes to  $N_{H2max}$ . So  $N_c$  is a characteristic hydrogen column density where the powerlaw increase in  $N_{H2}$  flattens off to form a plateau with the maximum value  $N_{H2max}$ . The profile in the lower panel of Fig. 7 was plotted using  $N_{H2max} = 7.5 \times 10^{20} \text{ cm}^{-2}$ ,  $N_c = 1.5 \times 10^{21} \text{ cm}^{-2}$  and  $\alpha = 2$ . We did not pursue any direct fitting of this profile using the fitted  $N_{Htot}$  values because of the difficulty of handling the upper limits for  $N_{H2}$  that arise when  $N_{HI}$  is low. Instead we performed a 3 dimensional grid search to find the best fit model which gave the least rms scatter for  $N_{H,i}$  across the 19 groups. At each grid point we fitted the 19 group spectra with 2 absorbing components,  $N_{H,i}$  and a fixed  $N_{H,g}$  including  $N_{H2}$  specified by values of the parameters  $N_{H2max}$ ,  $N_c$  and  $\alpha$ . Fig. 8 shows the result with  $N_{H2max} = 7.5 \times 10^{20} \text{ molecules cm}^{-2}$ ,  $N_c = 2.37 \times 10^{21} \text{ atoms cm}^{-2}$  and  $\alpha = 2$ . The scatter in  $N_{H,i}$  across the groups is now significantly reduced to rms 0.128 dex closer to the expected value of  $\approx 0.09$  dex. The reduced Chi-squared is  $\chi^2_\nu = 33.1$  while the expected value given the intrinsic scatter in  $N_{H,i}$  (rms 0.09 dex between the groups of 26 GRBs) is  $\langle \chi^2_\nu \rangle = 13.8$ . So some of the scatter in Fig. 8 most likely arises from errors in modelling the Galactic column density. The geometric mean value of  $N_{H,i}$  for the 19 groups in Fig. 8 is  $8.8 \times 10^{20} \text{ cm}^{-2}$  ( $z = 0.0$ ) which is a significantly lower than the value for the distribution in Fig. 1 ( $2.1 \times 10^{21} \text{ cm}^{-2}$ ) and very close to the mean in Fig. 5 and the value assumed to plot Fig. 7 ( $8.9 \times 10^{20} \text{ cm}^{-2}$ ). This is understandable since our estimate of the Galactic contribution to the absorption has now increased and the upper limits present in the fitting of individual sources have been eliminated using the groups.

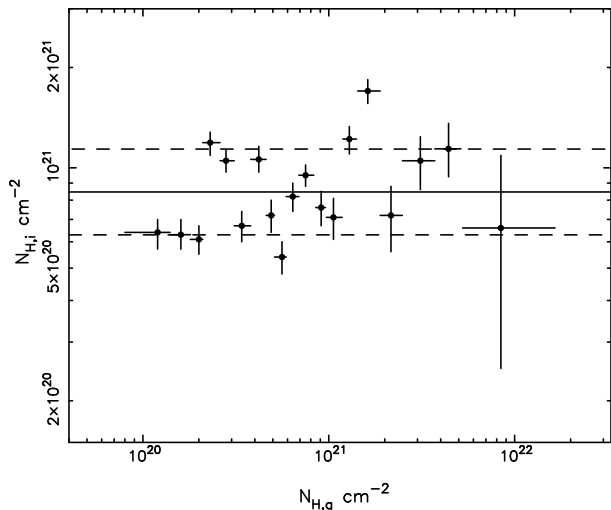


**Figure 8.** The  $N_{H,i}$  values for the 19 GRB groups using  $N_{H,g}$  from Equation 6 and using  $N_{H2}$  from Equation 5. The errors plotted for  $N_{H,i}$  are the 90% ranges. The horizontal lines are as in Fig. 2.

The estimated mean and rms scatter values of the excess component are plotted in Fig. 7 as the horizontal lines. They largely encompass the fitted  $N_{Htot}$  values for low  $N_{HI}$  where the excess column dominates. Finally, we note that the fitted values of  $N_{H2max}$  and  $N_c$  are dependent on the  $N_{HI}$  values used. Authors of the LAB survey and similar 21 cm surveys caution that saturation of the 21 cm emission may lead to inaccurate or under estimates of the atomic hydrogen column density when  $N_{HI} \gg 10^{21} \text{ cm}^{-2}$ . Correlation of the LAB 21 cm map with extinction maps (E(B-V) derived from IR emission, see next section) indicates that any saturation is not very significant until  $N_{HI} > 10^{22} \text{ cm}^{-2}$ . However, we acknowledge that some fraction of the column we are ascribing to  $H_2$  may actually be  $HI$  that has been lost due to such saturation.

### 3.3 Including dust extinction in the ISM modelling

So far we have not considered interstellar dust. Dust is relevant because it locks up some metals from the ISM, which are not therefore seen in gas phase abundance measurements. As noted previously, these metals still contribute to the soft X-ray absorption, albeit with some shielding due to the thickness of the grains. We assume that this absorption is already correctly accounted for (see also Section 4), but dust has an additional role in catalysing molecule formation, and we consider that process in this section. Most of the  $H_2$  in the ISM is probably created on the surface of dust grains. The production rate is dependant on the collision probability between H atoms and the grains and the amount of gaseous molecular material released will depend on the sticking probability of  $H_2$  on the grains. The competing dissociation rate depends on the temperature, cosmic ray and X-ray flux and collisions within interstellar shocks. For details the reader is referred to the full discussion in Shull & Beckwith (1982) and the references therein. For lines of sight out of the Galactic plane, with cold, low

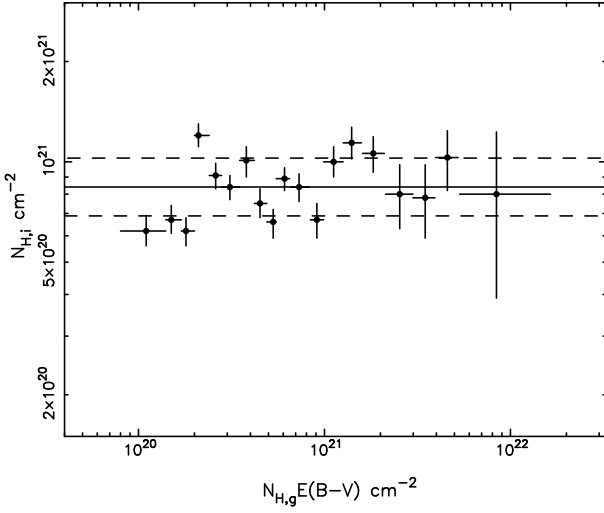


**Figure 9.** The  $N_{H,i}$  values for the 19 GRB groups using  $N_{H,g}$  from Equation 6 with  $N_{H_2}$  from Equation 7. The errors plotted for  $N_{H,i}$  are the 90% ranges. The horizontal lines are as in Fig. 2.

density material, we expect the  $N_{H_2}$  column density to be proportional to the product  $N_{HI}N_{dust}$ . As we move closer to the plane the density will increase although the ratio of  $N_{H_2}/N_{HI}$  will be variable depending on local conditions. The profile derived from our initial analysis, shown in Fig. 7, indicates that there is an upper limit to the local  $N_{H_2}$  of  $\sim 10^{21}$  molecules  $\text{cm}^{-2}$ , independent of  $N_{HI}$ .

We modified the functionality of the  $N_{H_2}$  profile so that it includes the extinction measure  $E(B - V)$ , using the all-sky maps of  $E(B - V)$  produced by Schlegel et al. (1998) from *IRAS* and *COBE/DIRBE* infra-red 100  $\mu\text{m}$  and 240  $\mu\text{m}$  data. These  $E(B - V)$  values are derived by correcting the measured IR emissivity using the measured temperature and assuming a constant reddening law so that  $E(B - V)$  is directly proportional to the dust column density,  $N_{dust}$ . In order to produce  $N_{HI}$  and  $E(B - V)$  values with the same limited angular resolution we rebinned the extinction maps into an all-sky Aitoff projection array with a pixel size of 0.75 degrees. This is identical to the array used by the FTOOLS NH procedure so we could use this to return both the LAB survey  $N_{HI}$  and  $E(B - V)$  values for every GRB position (or any other position). The molecular hydrogen column density profile was set as

$$N_{H_2} = N_{H_2max} \left[ 1 - \exp \left( \frac{-N_{HI}E(B - V)}{N_c} \right) \right]^\alpha. \quad (7)$$

Fitting the grouped spectra adopting this measure for  $N_{H_2}$  and, again, searching for values of the parameters  $N_{H_2max}$ ,  $N_c$  and  $\alpha$  which produced the minimum rms dex scatter gave the results shown in Fig. 9. The best fit parameters are  $N_{H_2max} = (7.2 \pm 0.3) \times 10^{20}$  molecules  $\text{cm}^{-2}$ ,  $N_c = (3.0 \pm 0.3) \times 10^{20}$  atoms  $\text{cm}^{-2}$  and  $\alpha = 1.1 \pm 0.1$  where the errors quoted were estimated from changes in  $\chi^2$  values calculated using the confidence ranges on  $N_{H,i}$  produced from the spectral fits (and plotted in Fig. 9). We note that the parameters which gave the minimum rms also gave the minimum  $\chi^2$ . The rms scatter in the fitted  $N_{H,i}$  values is now 0.087 dex, visibly less than for the distribution shown

Grouping	$N_{H,i}$	$\Gamma$	Norm
$37 \times 13 + 1 \times 12$	$1.06 \pm 0.07$	$1.87 \pm 0.16$	$7.06 \pm 2.38$
$25 \times 19 + 1 \times 18$	$0.85 \pm 0.05$	$1.84 \pm 0.13$	$7.00 \pm 1.90$
$18 \times 26 + 1 \times 25$	$0.84 \pm 0.02$	$1.83 \pm 0.12$	$6.85 \pm 1.75$
$17 \times 29$	$0.82 \pm 0.03$	$1.82 \pm 0.12$	$6.90 \pm 1.78$

**Table 1.** The mean and rms scatter of fitted spectral parameter values using different groupings with  $N_{H,g}$  from Equation 6 and  $N_{H_2}$  from Equation 7. The groupings are given as #bins $\times$ #GRBs per bin.  $N_{H,i}$   $10^{21} \text{ cm}^{-2}$  is the geometric mean of the excess column density (at  $z=0$ ). The photon index is  $\Gamma$  and the normalisation is Norm  $10^{-4} \text{ ph cm}^{-2} \text{ s}^{-1} \text{ keV}^{-1}$ .

in Fig. 8 and close to the value  $\approx 0.09$  dex expected from the original distribution obtained from the individual spectral fits. The reduced Chi-squared is now  $\chi_\nu^2 = 11.1$  while the expected value is  $\langle \chi_\nu^2 \rangle = 11.7$ . Including the molecular hydrogen column density in the ISM model using the profile given by Equation 7 has eliminated the unexpected trend in the fitted  $N_{H,i}$  values seen in Figs. 2 and 5.

In order to check that the results are not sensitive to the particular distribution of GRBs within the 19 groups used, we performed the analysis using different groupings. The mean and rms of the fitted parameters taken across the groups are given in Table 1. The mean photon indices and normalisations are reasonably constant. When the number of GRBs in each group is only 13 the scatter in the normalisations and excess column density values is largest, as expected. For the grouping plotted in Fig. 9,  $18 \times 26 + 1 \times 25$ , the scatter in excess column density is significantly lower. Increasing the group size further to 29 makes little difference although the scatter is now starting to increase. This is because some of the groups now span too large a range in Galactic absorption, a factor of 2 to 3, and using a single, fixed value for  $N_{H,g}$  is no longer a good approximation for the combined spectra. The results are clearly not sensitive to the particular GRB groupings used although the chosen grouping gives the best compromise between using too few GRBs per group and getting a large scatter in  $N_{H,i}$  and using too many GRBs per group and losing resolution in  $N_{H,g}$ .

We repeated this analysis using the trial1 and trial2 XRT calibrations described in Section 2. The best fit parameter values were the same within the quoted errors. The rms scatter was larger, 0.090 dex using trial1 and 0.13 using trial2. The only really significant difference was the geometric mean of  $N_{H,i}$  across all the groups. In Fig. 9 this is  $8.4 \times 10^{20} \text{ cm}^{-2}$  whereas using the trial1 calibration gave  $1.05 \times 10^{21} \text{ cm}^{-2}$  some 25% higher and using trial2 gave  $0.66 \times 10^{21} \text{ cm}^{-2}$ , 22% lower.

#### 4 COMPARISON OF THE $N_{H_2}$ DISTRIBUTION WITH OTHER MEASUREMENTS

How does the molecular hydrogen column density profile inferred from GRB afterglow X-ray spectra compare with other measurements? Fig. 10 shows the molecular hydrogen column measured in UV absorption to stars taken from Savage et al. (1977) (74 objects), Rachford et al. (2002, 2009) (38 objects) and 66 extragalactic high latitude sources taken from Wakker (2006). The molecular hydrogen column



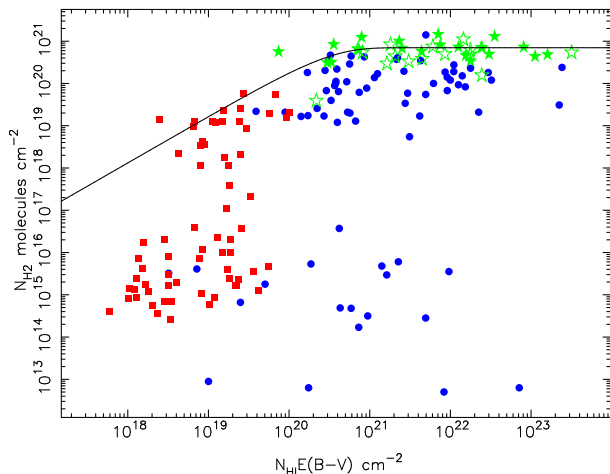


**Figure 10.** The molecular hydrogen column as a function of  $N_{HI}E(B-V)$ . The *Copernicus* measurements from Savage et al. (1977) are plotted as blue circles (sources with only upper limits for  $N_{H_2}$  are not included). The *FUSE* measurements from Rachford et al. (2002,2009) are plotted as green stars/open stars and the extragalactic *FUSE* measurements from Wakker (2006) are plotted as red squares. The solid line is the profile inferred from the X-ray GRB afterglow spectra.

density is plotted as a function of  $N_{HI}E(B-V)$  derived from the LAB survey and *IRAS* and *COBE/DIRBE* extinction maps in the same way as described above for implementing the  $N_{H_2}$  profile (Equation 7). The profile derived from the X-ray absorption in GRB afterglows forms a reasonably well defined upper envelope to the distribution of  $N_{H_2}$  points. The plateau for  $N_{HI}E(B-V) > N_c$  is well matched between the UV and X-ray confirming that  $N_{H_2}$  is independent of the atomic column density and the dust extinction in the Galactic plane. There is clearly a very large range of UV measured values below the upper envelope. The X-ray absorption measurements suggest that a large fraction of the molecular hydrogen is not seen in the UV absorption spectra. This may be because the absorption line features seen in the UV are produced by dense clouds of gas which have a well defined velocity with little dispersion. For many lines of sight through the galaxy a significant fraction of the molecular hydrogen may be distributed at much lower density and with significant velocity dispersion. This material would produce very broad absorption features in the UV spectra or possibly a large number of small line features at different velocities which cannot be detected or identified. Most of the *FUSE* observations of bright sources reported by Rachford et al. (2002, 2009) are close to the X-ray profile indicating that when the signal to noise and sensitivity are good all the molecular hydrogen can be detected in UV absorption. It is possible that some of these bright *FUSE* sources are not subject to the entire Galactic column density. This might explain why two sources, HD 164740 and HD 186994, have  $N_{H_2}$  values significantly lower than predicted by the model.

The *FUSE* source which is closest to a GRB position is HD154368, 0.86 degrees from GRB 100504A. For this GRB the  $N_{H,g}$  is  $2.6 \times 10^{21} \text{ cm}^{-2}$  and the fitted  $N_{H,i}$  is  $3.8 \times 10^{21} \text{ cm}^{-2}$ . This is consistent with the *FUSE* result of  $N_{H_2} = 1.45 \times 10^{21} \text{ cm}^{-2}$ . The next closest is HD40893, 1.64

degrees from GRB 061019. In this case  $N_{H,g} = 3.8 \times 10^{21} \text{ cm}^{-2}$  and the fitted  $N_{H,i}$  is  $8.4 \times 10^{21} \text{ cm}^{-2}$  consistent with the *FUSE* value of  $N_{H_2} = 3.80 \times 10^{20} \text{ cm}^{-2}$ . *FUSE* source HD206267 is 1.71 degrees from GRB 050422 and *FUSE* source HD179406 is 1.77 degrees from GRB 060105 but these separations are now significant compared with the resolution and variations in the  $N_{HI}$  and  $E(B-V)$  maps. All other *FUSE* sources are several degrees or more from the nearest GRB and any stacking analysis to try and make a more detailed comparison is not possible.

Emission from the lower frequency rotational transitions of carbon monoxide (CO) molecules in the radio band (the  $J=1 \rightarrow 0$  line is at 115 GHz) is used as a proxy for  $H_2$  in studies of Giant Molecular Clouds, (see e.g. Dickman (1978) and Glover & Mac Low (2011)). A simple conversion factor  $X_{CO} = N_{H_2}/W_{CO} \simeq 2 \times 10^{20} \text{ cm}^{-2} \text{ K}^{-1} \text{ km}^{-1} \text{ s}$ , where  $W_{CO} \text{ K km s}^{-1}$  is the intensity of the CO emission line ( $J=1 \rightarrow 0$ ) integrated over velocity, is used to predict the  $N_{H_2}$  column density of a cloud from the observed  $W_{CO}$ . The density of the absorbing column can be estimated independently by various means: from the diffuse  $\gamma$ -ray flux produced by interactions with cosmic rays, from the measured extinction or from the atomic hydrogen 21 cm emission, but the presence of  $H_2$  is inferred and not observed directly.

We attempted to use such a scaling by rebinning the CO survey data from Dame et al. (2001)<sup>2</sup> to produce a CO map in the same Aitoff projection used by the FTOOLS NH procedure (as we did for the  $E(B-V)$  mapping described above). We extracted  $W_{CO}$  values for every GRB position and used these to set  $N_{H,g} = N_{HI} + 2X_{CO}W_{CO}$  in the fitting of the group spectra. The extended CO survey covers  $\sim 60\%$  of the sky so we assumed that  $W_{CO} = 0$  for GRBs which fell outside this area. This is reasonable because those sky areas not covered by the survey are known to be regions of very low CO emission. We were unable to find a scaling factor  $X_{CO}$  which reduced the rms scatter across the 19 groups. In retrospect this is not surprising because the profile of the molecular fraction ( $f(H_2)$  defined by Equation 4) predicted using the CO maps is very scattered and not peaked around  $N_{H,tot} \simeq 2 \times 10^{21} \text{ cm}^{-2}$  as required. In fact there is no correlation between  $N_{H_2}$  given by Equation 7 and  $W_{CO}$ . CO emission may be a proxy for molecular hydrogen in dense molecular clouds but this does not seem to extend to the ISM distribution across the Galaxy. We searched for other potential correlations between  $W_{CO}$  and the dust or hydrogen column densities. We found that by far the best correlation was with the dust-to-hydrogen ratio defined by

$$R_{DH} = \frac{E(B-V) \times 10^{22}}{N_{HI} + 2N_{H_2}} \quad (8)$$

The factor of  $10^{22}$  is included so that the ratio has a value  $\sim 1$  out of the Galactic plane and Equation 7 was used to calculate  $N_{H_2}$ . This ratio is plotted as a function of  $W_{CO}$  in Fig. 11. For the bottom panel we calculated the average ratio values in 20 bins across the full  $W_{CO}$  range. These average values increase monotonically with  $W_{CO}$  (within the noise) and are well fitted by the function

<sup>2</sup> Thomas Dame kindly provided us with the mid-latitude extension of the CfA CO survey prior to publication and this gave us better coverage out of the Galactic Plane.

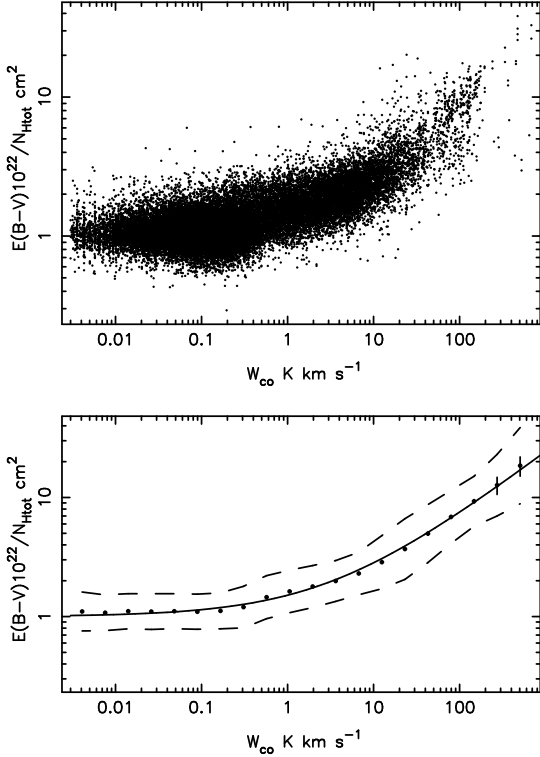


**Figure 11.** The dust-to-hydrogen ratio,  $R_{DH}$ , as a function of CO emission. Top panel: Each point represents a pixel  $\approx 0.6$  deg<sup>2</sup>.  $W_{CO}$  values are available and plotted for  $\sim 60\%$  of the sky. Bottom panel: Average  $R_{DH}$  values calculated for 20 logarithmic bins across the full range of  $W_{CO}$ . The dashed lines indicate the 90% range of the scatter in  $R_{DH}$ . Error bars are plotted for the averages but these are too small to see except for the bins at the top end. The solid line is the model fit described in the text.

$$R_{DH} = 1 + A \times W_{CO}^\gamma \quad (9)$$

where  $A = 0.51 \pm 0.04$  and  $\gamma = 0.55 \pm 0.03$ . This function fit is plotted in Fig. 11. The correlation is still present if the molecular hydrogen component is ignored but the scatter is significantly reduced when the  $N_{H_2}$  term is included.

The dust-to-hydrogen ratio is important in the context of the X-ray absorption model of the Galaxy. As defined by Equation 9 the ratio changes from 1.0 out of the Galactic plane to a peak of  $\sim 20$  in the Galactic plane. This increase could be due to a change in metallicity and imply a gradient of the abundances of  $A_Z$  in Equation 3 or it could reflect a change in the fraction of the higher metallicity material condensed into dust thereby representing a change in the  $\beta_{Z,i}$  values in the same Equation. We have tested both these possibilities by introducing, in turn, an abundance gradient and a gas depletion gradient into the absorption model used for the spectral fitting of the GRB groups. We only varied these factors for the elements expected to be incorporated into the dust (C, O, Na, Mg, Al, Si, S, Cl, Ca, Cr, Fe, Co, Ni for which the gas depletion can be set in the `tbvarabs` routine in `XSPEC`). The group spectral fits are sensitive to the abundances: a change of just 20% in abundance over the full hydrogen column density range (i.e.  $\pm 10\%$  about the average given by Wilms et al. (2000)) is sufficient to significantly degrade the quality of the best fit model shown in

Fig. 9. The opposite is true for the gas depletion factors. If they are set to the extreme value of 1.0 (no dust) then the quality of the fit degrades but the changes are barely statistically significant. Using a value of 0.0 (all dust) introduces an even smaller degradation. This is because changing the gas depletion does not alter the amount of material in the column but simply changes the shielding effect of the dust grains and this effect is small. We conclude that the change in  $R_{DH}$  must be dominated by gas depletion and not an abundance gradient although the X-ray absorption measurements from the GRB afterglows are unable to confirm the range in gas depletion implied by  $R_{DH}$  shown in Fig. 11. As already demonstrated, the spectral fitting of the grouped GRB afterglow spectra serves as a good calibration of the elemental abundances assumed. A study of Galactic absorption using the afterglow spectra from GRBs, described by Watson (2011), concludes that the metallicity of a typical Galactic line of sight is not consistent with the abundances given by Wilms et al. (2000). However, if the molecular hydrogen column density is included in the absorption model, we have shown that these abundances are correct to within  $\sim \pm 10\%$  and there is no evidence for a large abundance gradient as a function of hydrogen column density.

In general as  $W_{CO}$  increases so the dust extinction,  $E(B - V)$ , and hydrogen column density,  $N_{Htot}$ , increase, but the dust-to-hydrogen ratio given by Equation 9 leads to a rather counter-intuitive result: if  $W_{CO} > 10$  K km s<sup>-1</sup> then  $R_{DH} \simeq 0.5W_{CO}^{0.55}$ . If we measure the dust extinction and CO emission then we can estimate the total hydrogen column density as  $N_{Htot} \simeq 2 \times 10^{22} E(B - V) W_{CO}^{-0.55}$  cm<sup>-2</sup>.

The well known correlation between the dust column density (given by  $E(B - V)$  or  $A_V = R_V E(B - V)$ ) and the hydrogen column (given by  $N_{HI}$ ) is better represented using  $N_{Htot}$ , including the molecular hydrogen component. The  $A_V - N_{Htot}$  relation has a fractional rms scatter of  $\sim 26\%$ , less than the  $A_V - N_{HI}$  relation for which the fractional rms scatter is  $\sim 33\%$ . Because the dust-to-hydrogen ratio,  $R_{DH}$ , increases with  $N_{Htot}$  the relationship is not linear. If  $E(B - V) < 0.1$ , and adopting  $R_V = 3.1$  from Watson (2011), then we find the linear relation  $N_{Htot} = 3.2 \times 10^{21}$  cm<sup>-2</sup>  $A_V$  but for  $E(B - V) > 0.1$  the correlation flattens off as  $R_{DH}$  increases. If we ignore the molecular hydrogen we find  $N_{HI} = 2.0 \times 10^{21}$  cm<sup>-2</sup>  $A_V^{0.86}$  a result very similar to the non-linear relationship given by Watson (2011). However, this non-linearity is introduced because of the missing molecular hydrogen component and the change in  $R_{DH}$  and is not a consequence of a gradient in metallicity.

## 5 THE MOLECULAR HYDROGEN FRACTION

We can calculate the molecular hydrogen fraction using all the pixels in the FTOOLS version of the LAB survey all-sky image and the rebinned version of the  $E(B - V)$  data from Schlegel et al. (1998). The result is plotted as a function of the total hydrogen column density in Fig. 12. Each point represents an estimate of molecular hydrogen fraction for a sky area of  $\approx 0.6$  deg<sup>2</sup>. The scatter is introduced because there is considerable scatter in the correlation between  $N_{HI}$  and  $E(B - V)$ . At high column densities the molecular hydrogen fraction actually decreases and the scatter gradually disappears because the  $N_{H_2}$  column density asymptotes to the

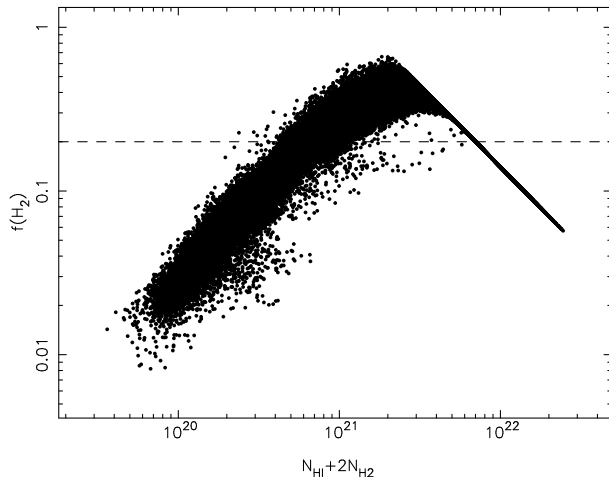


**Figure 12.** The molecular hydrogen fraction plotted as a function of the total hydrogen column density calculated for pixels across the whole sky. The horizontal line represents the 20% level which is the default value in the XSPEC tbabs routine.

constant value,  $N_{H_2max}$ . Conversely, for low total hydrogen column densities the molecular hydrogen density is increasing faster than the total column density and we get a peak in the  $f(H_2)$  profile. The presence of the peak in the  $f(H_2)$  distribution is why the introduction of this model is able to improve the fitting of the GRB afterglow group spectra. It has the effect of significantly increasing the absorption at and around  $N_{HI} = 10^{21} \text{ cm}^{-2}$  while having relatively little impact on the absorption at high and low  $N_{HI}$  values. The model using the product  $N_{HI}E(B-V)$  rather than just  $N_{HI}$  alone offers an improvement because the correlation between  $N_{HI}$  and  $E(B-V)$  is not tight and the molecular hydrogen column depends on both  $N_{HI}$  and  $E(B-V)$ . The constant value of 20% used in the XSPEC tbabs routines is shown in Fig. 12 as the horizontal dashed line whereas we find the maximum value of  $N_{H_2}$  is  $\sim 66\%$ . Remarkably the mean value of  $f(H_2)$  produced by the current model over the sky is 20.2%, very close to the value adopted by Wilms et al. (2000).

Why does the molecular hydrogen fraction peak at  $N_{Htot} \approx 2 \times 10^{21} \text{ cm}^{-2}$  rather than continuing to rise as you might expect and why is the  $N_{H_2}$  column density not correlated with the CO emission? We don't know, but we comment that the formation and destruction of molecular species is dependent on many factors. Theoretical and observational studies of molecular clouds indicate that the formation of  $H_2$  is primarily determined by the time available for its formation and the  $X_{CO}$  factor relating the presence of  $H_2$  to the CO emission can be highly variable if the metallicity and density are low and the background UV radiation field is high (Glover & Mac Low (2011); Shetty et al. (2011)). The  $N_{H_2}$  column density model for the Galaxy presented here reflects the average state of the ISM of the Galaxy rather than conditions in molecular clouds taken individually. There is a large scatter in both the molecular hydrogen fraction and the dust-to-hydrogen ratio which must reflect a broad spectrum of local conditions.

## 6 CONCLUSION

Measurements of X-ray absorption in the spectra of GRB afterglows indicate that using the distribution of  $HI$  as the only direction dependent variable in the model of the Galactic ISM is inadequate to describe variations in the column density seen. The discrepancy can be explained by including a molecular hydrogen column density component which is a function of the product of the  $HI$  column density and dust extinction,  $N_{HI}E(B-V)$ , given by Equation 7. The distribution of molecular hydrogen inferred from the X-ray absorption measurements is in agreement with direct measurements of the  $N_{H_2}$  column density made using UV absorption spectra. Summing the column densities of atomic and molecular hydrogen we can estimate the total hydrogen column density and calculate a dust-to-hydrogen ratio,  $R_{DH}$ . This ratio is shown to correlate with the CO emission following the function given by Equation 9. In principle  $R_{DH}$  can be used to estimate the gas depletion factors in the X-ray absorption model although the present X-ray absorption measurements are not sensitive enough to warrant the inclusion of this direction dependence.

If the total effective hydrogen column density (at  $z = 0$ ) is less than  $\sim 1.5 \times 10^{21} \text{ cm}^{-2}$  then the systematic error on the fitted value, imposed by current uncertainties in the area calibration of the *Swift* XRT, is  $\sim 16\%$ . For higher column densities this systematic error drops to  $\sim 8\%$ . Furthermore, we can confirm that the elemental abundances in the Galaxy assumed in Wilms et al. (2000) are correct to within  $\sim \pm 10\%$  although because of the limited spectral resolution of the CCD detector the XRT is not sensitive to the details of the ratios between the individual elements.

If you required an accurate estimate of the X-ray absorbing column density in our Galaxy you should include an estimate of the molecular hydrogen column density<sup>3</sup>. When using the tbabs in XSPEC you should, at the very least, multiply the atomic hydrogen column density estimated from 21 cm survey data,  $N_{HI}$ , by a factor of 1.25 so that 20% of the total hydrogen column is molecular. You can improve the accuracy by employing Equation 5, calculating the total column using Equation 6 and setting the molecular fraction appropriately using the tbvarabs model. If you have a Galactic  $E(B-V)$  extinction measure for the source position you can further improve the accuracy using the  $N_{H_2}$  profile given in Equation 7.

## ACKNOWLEDGEMENTS

We gratefully acknowledge funding for *Swift* at the University of Leicester by the UK Space Agency and thank Thomas Dame for giving us access to the extended CO survey data which have not yet been published. RLCS is supported by a Royal Society Dorothy Hodgkin Fellowship.

<sup>3</sup> Software to calculate  $N_{H_2}$  and  $N_{Htot}$  for a given position is available at <http://www.star.le.ac.uk/~rw/xabs>

## REFERENCES

- Anders E., Grevesse N., 1989, *Geochim. Cosmochim. Acta*, 53, 197
- Arnaud K. A., 1996, in *Astronomical Society of the Pacific Conference Series*, Vol. 101, *Astronomical Data Analysis Software and Systems V*, G. H. Jacoby & J. Barnes, ed., p. 17
- Behar E., Dado S., Dar A., Laor A., 2011, *ApJ*, 734, 26
- Campana S., Mangano V., Blustin A. J., Brown P., Burrows D. N., Chincarini G., Cummings J. R., Cusumano G., Della Valle M., Malesani D., Mészáros P., Nousek J. A., Page M., Sakamoto T., Waxman E., Zhang B., Dai Z. G., Gehrels N., Immler S., Marshall F. E., Mason K. O., Moretti A., O’Brien P. T., Osborne J. P., Page K. L., Romano P., Roming P. W. A., Tagliaferri G., Cominsky L. R., Giommi P., Godet O., Kennea J. A., Krimm H., Angelini L., Barthelmy S. D., Boyd P. T., Palmer D. M., Wells A. A., White N. E., 2006, *Nature*, 442, 1008
- Campana S., Salvaterra R., Melandri A., Vergani S. D., Covino S., D’Avanzo P., Fugazza D., Ghisellini G., Sbarufatti B., Tagliaferri G., 2012, *MNRAS*, 421, 1697
- Dame T. M., Hartmann D., Thaddeus P., 2001, *ApJ*, 547, 792
- Dickman R. L., 1978, *ApJS*, 37, 407
- Froebrich D., Davis C. J., Ioannidis G., Gledhill T. M., Takami M., Chrysostomou A., Drew J., Eisloffel J., Gosling A., Gredel R., Hatchell J., Hodapp K. W., Kumar M. S. N., Lucas P. W., Matthews H., Rawlings M. G., Smith M. D., Stecklum B., Varricatt W. P., Lee H. T., Teixeira P. S., Aspin C., Khanzadyan T., Karr J., Kim H.-J., Koo B.-C., Lee J. J., Lee Y.-H., Magakian T. Y., Movsessian T. A., Nikogossian E. H., Pyo T. S., Stanke T., 2011, *MNRAS*, 413, 480
- Gehrels N., Chincarini G., Giommi P., Mason K. O., Nousek J. A., Wells A., White N. E., Barthelmy S. D., Burrows D. N., Cominsky L. R., Hurley K. C., Marshall F. E., Mészáros P., Roming P. W. A., Angelini L., Barbier L. M., Belloni T., Campana S., Caraveo P. A., Chester M. M., Citterio O., Cline T. L., Cropper M. S., Cummings J. R., Dean A. J., Feigelson E. D., Fenimore E. E., Frail D. A., Fruchter A. S., Garmire G. P., Gendreau K., Ghisellini G., Greiner J., Hill J. E., Hunsberger S. D., Krimm H. A., Kulkarni S. R., Kumar P., Lebrun F., Lloyd-Ronning N. M., Markwardt C. B., Mattson B. J., Mushotzky R. F., Norris J. P., Osborne J., Paczynski B., Palmer D. M., Park H.-S., Parsons A. M., Paul J., Rees M. J., Reynolds C. S., Rhoads J. E., Sasseen T. P., Schaefer B. E., Short A. T., Smale A. P., Smith I. A., Stella L., Tagliaferri G., Takahashi T., Tashiro M., Townsley L. K., Tueller J., Turner M. J. L., Vietri M., Voges W., Ward M. J., Willingale R., Zerbi F. M., Zhang W. W., 2004, *ApJ*, 611, 1005
- Glover S. C. O., Mac Low M.-M., 2011, *MNRAS*, 412, 337
- Kalberla P. M. W., Burton W. B., Hartmann D., Arnal E. M., Bajaja E., Morras R., Pöppel W. G. L., 2005, *A&A*, 440, 775
- Mészáros P., Rees M. J., 1992, *MNRAS*, 257, 29P
- Page K. L., Starling R. L. C., Fitzpatrick G., Pandey S. B., Osborne J. P., Schady P., McBreen S., Campana S., Ukwatta T. N., Pagani C., Beardmore A. P., Evans P. A., 2011, *MNRAS*, 416, 2078
- Rachford B. L., Snow T. P., Destree J. D., Ross T. L., Ferlet R., Friedman S. D., Gry C., Jenkins E. B., Morton D. C., Savage B. D., Shull J. M., Sonnentrucker P., Tumlinson J., Vidal-Madjar A., Welty D. E., York D. G., 2009, *ApJS*, 180, 125
- Rachford B. L., Snow T. P., Tumlinson J., Shull J. M., Blair W. P., Ferlet R., Friedman S. D., Gry C., Jenkins E. B., Morton D. C., Savage B. D., Sonnentrucker P., Vidal-Madjar A., Welty D. E., York D. G., 2002, *ApJ*, 577, 221
- Ride S. K., Walker Jr. A. B. C., 1977, *A&A*, 61, 339
- Sari R., Piran T., Narayan R., 1998, *ApJ*, 497, L17
- Savage B. D., Bohlin R. C., Drake J. F., Budich W., 1977, *ApJ*, 216, 291
- Schady P., Savaglio S., Krühler T., Greiner J., Rau A., 2011, *A&A*, 525, A113
- Schlegel D. J., Finkbeiner D. P., Davis M., 1998, *ApJ*, 500, 525
- Shetty R., Glover S. C., Dullemond C. P., Ostriker E. C., Harris A. I., Klessen R. S., 2011, *MNRAS*, 415, 3253
- Shull J. M., Beckwith S., 1982, *ARA&A*, 20, 163
- Starling R. L. C., Page K. L., Pe’er A., Beardmore A. P., Osborne J. P., 2012, *MNRAS*, 427, 2950
- Starling R. L. C., Wiersema K., Levan A. J., Sakamoto T., Bersier D., Goldoni P., Oates S. R., Rowlinson A., Campana S., Sollerman J., Tanvir N. R., Malesani D., Fynbo J. P. U., Covino S., D’Avanzo P., O’Brien P. T., Page K. L., Osborne J. P., Vergani S. D., Barthelmy S., Burrows D. N., Cano Z., Curran P. A., de Pasquale M., D’Elia V., Evans P. A., Flores H., Fruchter A. S., Garnavich P., Gehrels N., Gorosabel J., Hjorth J., Holland S. T., van der Horst A. J., Hurkett C. P., Jakobsson P., Kamble A. P., Kouveliotou C., Kuin N. P. M., Kaper L., Mazzali P. A., Nugent P. E., Pian E., Stamatikos M., Thöne C. C., Woosley S. E., 2011, *MNRAS*, 411, 2792
- Wakker B. P., 2006, *ApJS*, 163, 282
- Watson D., 2011, *A&A*, 533, A16
- Wilms J., Allen A., McCray R., 2000, *ApJ*, 542, 914
- Zafar T., Watson D. J., Tanvir N. R., Fynbo J. P. U., Starling R. L. C., Levan A. J., 2011, *ApJ*, 735, 2